Journal of Thermal Engineering
https://jten.yildiz.edu.tr/
https://doi.org/10.47481/jten.0070

RESEARCH ARTICLE

Gravity driven film flow and surface heat transfer characteristics around horizontal tube

Awdhesh Kumar Poddar[1,*], Nirmal Kant Singh[2]

[1]Department of Mechanical Engineering, National Institute of Technology, Kurukshetra, 136119, HR, India
[2]Department of Mechanical Engineering, National Institute of Technology, Kurukshetra, 136119, HR, India

Abstract

Horizontal tube liquid-driven evaporators find widespread application in industries such as chemicals, textiles, and food processing. In evaporative heat exchangers, heat transfer variables around the horizontal round tube inherently fluctuate. Significant variations in film thickness are observed in the upper and lower regions of the tube. Employing a transient liquid surface tracking technique, focusing on the interface of two immiscible phases, is crucial. This paper conducts an insightful study to analyze the surface heat transfer and hydrodynamic behavior of gravity driven film flow, considering various factors such as geometrical arrangements, liquid flow rate (Ref = 850, 1050 & 1250), and flow fluctuations. The influence of film thickness is investigated by a Volume of Fluid (VOF) model implemented in ANSYS CFD software. The results, validated against Nusselt (1916) correlations and experiments conducted by researchers documented in the literature, indicate that the maximum error in simulations is limited to 6%.

Keywords: Heat exchanger, horizontal tubes, film thickness, surface heat transfer coefficient

Cite this article as: Poddar, A. K., & Singh, N. K. (2026). Gravity driven film flow and surface heat transfer characteristics around horizontal tube. Journal of Thermal Engineering, 12(5), 1848–1858. https://doi.org/10.47481/jten.0070

1. Introduction

In falling film tubular heat exchangers, evaporative heat transfer takes place as a process of fluid flows over the internally heated tubes. In these heat exchangers, an enhanced heat transfer can be achieved with only a small temperature difference. Falling film evaporation plays a crucial role in fulfilling the requirements of recent technological demands, especially in the pharmaceutical sector, food processing industry and desalination plants. Figure 1 presents a schematic overview of a falling film evaporative heat exchanger (FFEHE), where inline horizontal cylinders are fixed at equal spacing and liquid sprinklers are placed above the cylinders, the flow being regulated by a regulating valve.

[1] carried out one of the earliest studies offering insights into the application of falling-film evaporators to the dairy industry. [2] investigated the rate of heat transfer process of a gravity-driven liquid film on flat tubes. They observed that the temperature of falling water depends upon the surrounding condition also. The surrounding humidity, air velocity and tube spacing affect the film evaporation. Based on their experiments an empirical correlation has been set to calculate the evaporative fluid cooling. The microscopic surface texture of the tube and its geometrical configuration present a promising area of research. Numerous renowned researchers have conducted both theoretical and experimental investigations to optimize operating temperature ranges, flow rates, tube arrangements and spacing, and sprinkler heights, all of which directly impact heat transfer performance. [3] performed an experimental analysis to examine the effect of vapour flow over a flat round tube bundle using refrigerant R134a in falling film evaporation. They investigated that the rate of flow acts as a significant factor which directs the surface heat transfer quantity. The liquid film heat transfer coefficient is influenced by the thickness of the flowing liquid film.

[4] contributed significantly to industrial applications like dairy industries and juice evaporators. [5] employed a laser measurement technique to determine the liquid film thickness on the tube surface and assess the heat transfer. The investigation presented in the paper aligns well with the non-intrusive

*Corresponding Author
E-mail Adress: akpm25@gmail.com

Submitted: 4 July 2025; **Accepted:** 24 December 2025

This paper was recommended for publication in revised form by Editor-in-Chief Ahmet Selim Dalkılıç

optical measurement technique and agrees with the classical correlation proposed by [6]. This optical measurement technique has been developed to enhance accuracy by avoiding direct contact with the formed liquid film over the tube exterior; this led to more precise results regarding the film thickness over the surface of tubes. In the primary stages of research, the film depth was obtained using a micrometer technique, revealing a consistency with the [6] correlation.

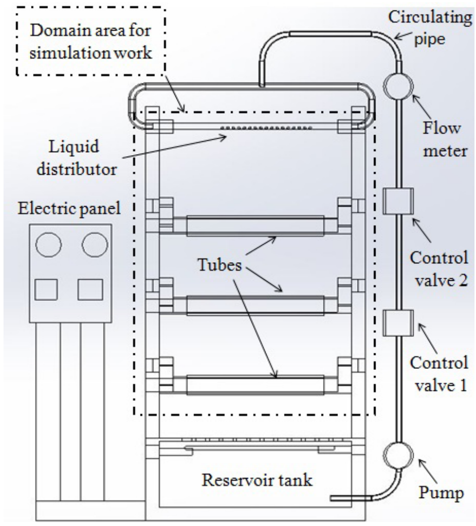

Figure 1. Schematic representation of a falling film heat exchanger

An investigation conducted by [7], explored two geometric configurations, with in-line horizontal tubes and staggered tube arrangements, revealing that rectangular pitch arrangements yielded superior heat transfer coefficient. Thickness measurement techniques (Optical Interferometry, X-ray Reflectometry (XRR), Spectroscopic Reflectometry, Capacitance and Optical Measurement) have been employed and rigorously validated for measuring the spectrum of film thickness, by [8–13].

[14] conducted a benchmark experimental study aimed at enhancing the rate of heat transfer characteristics in FFEHE, comparing the structure and even surfaces of tube bundles. Investigations conducted by [15,16] showed that the rolled work tubes have a higher heat transfer coefficient, equated with smooth tubes. Beyond varying geometrical arrangements, constraints such as pitch of tubes, sprinkler height, and rate of flow etc., have also been a crucial point for research. [17] conducted a numerical simulation of liquid film thickness around the horizontal tube. An experimental and numerical study conducted by [18,19] focused on enhancing heat transfer using annular ribs inside a tube. The results revealed that the ribbed tube exhibited a higher heat transfer rate compared to the smooth tube, along with an improved performance factor under turbulent flow conditions.

[20] employed a multiphase Volume of Fluid (VOF) approach to observe the effects of film thickness and heat transfer coefficient on tube ellipticity, Reynolds number, inlet thermodynamic conditions, and seawater salinity. The objective of this numerical analysis is to investigate the fluctuating behavior of flow features to gain insight into the fundamentals of flow hydrodynamics. [21] provided a review focusing on research related to FFEHE frequently used in desalination systems, particularly in multi-effect distillation (MED) systems. The review covers topics such as methods of falling-film evaporation, system operation, and challenges related to scaling. [22] investigated numerically and revealed that falling film flow plays a crucial role in determining the shell-side heat transfer characteristics of spiral-wound heat exchangers. The study also highlighted that the liquid surface adhesion over the tube surface significantly influences the characteristics of the falling liquid film flow.

Several recent investigations have focused on improving heat exchanger performance through the strategic application of vortex generators, flow deflectors, and engineered surface morphologies [23–25]. The performance of heat exchangers has also been investigated by incorporating nanofluids as the working medium by [25–28]. [28] provides an inclusive review of developments in predicting flow pattern transitions, fluid thickness, heat transfer, and liquid film rupture in falling films over a flat array of tubes. [29] conducted a study on 2-D external falling film evaporation on micro-ribbed tube surfaces. The research focused on examining how different structural parameters of the micro-ribs influence the flow behavior and heat transfer phenomena of the exterior falling film, with the goal of identifying the optimum tube configuration for various operating conditions.

In the current simulation, a multiphase flow analysis using ANSYS (Fluent), a Computational Fluid Dynamics (CFD) software, is conducted. The Volume of Fluid (VOF) technique is employed to manage multiphase flow and detect the boundary between the two immiscible fluids. The numerical investigation is primarily validated against available data in the literature and then extended to examine the effects of geometrical and flow parameters on falling film thickness around the circumference of evaporative heat exchangers. To minimize experimental costs, simulation analyses within acceptable ranges have been employed, enhancing their applicability in future studies. The novelty of the present work lies in examining a wider range of flow conditions across different tube diameters, offering deeper insights into the underlying flow physics. The study incorporates improved mesh resolution, an enhanced boundary-condition strategy, a more robust validation procedure, and higher-quality flow visualizations. Together, these advancements clearly distinguish in the investigation.

2. Problem formulation

A set of two in-line horizontal circular cylinders is arranged for investigation. Liquid spray is directed onto a horizontal tube from a distributor array, propelled by gravity, and establishes a liquid film over the tube's exterior. This liquid film spreads circumferentially until it completely covers the tube's surface. Accumulating at the bottom of the tube, the liquid forms a column and then flows onto the next tube. Gravity, surface cohesion, viscous forces, and inertial forces collectively influence the progression of liquid film spreading. To ensure uninterrupted flow formation, the extreme left side of the simulation domain is set equal to the tube's diameter. However, the distributor hole diameter is influenced by aspects such as liquid properties, operating conditions, tube diameter, and the required flow distribution, and it is generally maintained within the range of 1–5 mm. In this simulation, the distributor hole diameter is set to 3 mm. For flow analysis, the tube diameter is maintained at 19.05 mm, with a spacing of 6.4 mm. The flow variables are examined corresponding to film Reynolds numbers of 850, 1050 and 1250. The selection of these film Reynolds numbers is based upon the typical operating range observed in film flow analysis. The simulation is further extended in the second phase to include heat interaction. For comparison with other geometrical parameters, an additional tube diameter of 25.05 mm is selected, and the flow variable is extended to 1250. The film Reynolds number is defined as $Re_f = 4\Gamma/\mu_l$ and the values considered here are 850, 1050, and 1250. Here, Γ represents the mass movement rate per unit width (kg/m·s), and μ_L is the dynamic viscosity of the flowing fluid (N·s/m²).

3. Meshing and boundary conditions

The boundary conditions imposed on the flow domain to capture the dynamic behavior of thin film flow are shown in Figure 2. The exterior surface of the tube wall is set as a zero-velocity boundary condition also known as no-slip boundary condition, the inlet section of the flow is designated as a velocity inlet, the outermost flow domain is set as a free flow and thus considered as a pressure inlet boundary condition, and the pressure at the exterior of the flow field is static, hence boundary condition assigned as a pressure outlet. The investigation initially focuses on studying the instable behavior of the liquid film around the tube without heat interaction, followed by further analysis incorporating energy interaction.

To enhance the efficiency of the simulation process, the flow domain is subdivided into two symmetrical parts that are symmetric about the Y-axis. Consequently, similar parts of the tubes are assigned symmetric boundary conditions.

The generated mesh aligns precisely with the specifications of the numerical solver used, ensuring smooth integration with the simulation software to effectively utilize the mesh and produce reliable results. It plays a crucial role in simulation analysis and should be robust enough to capture all the necessary parameters and meet specified convergence criteria. The mesh is illustrated in Figure 3 (a), (b) & (c), offering a detailed view of the mesh to assess its quality. An inflation technique is applied over adjacent to the surface over the tube, enabling it to capture a minute variation in this highly sensitive zone. This involves a progressive increase in grid size along the tube surfaces, facilitating an easy and precise capture of flow parameters. The generated mesh is quadrilateral structured and becomes finer near the wall, enabling the effective capture of small fluctuations.

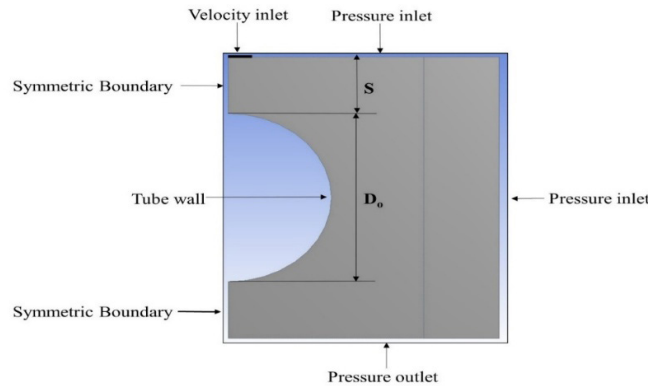

Figure 2. Boundary conditions and the flow domain

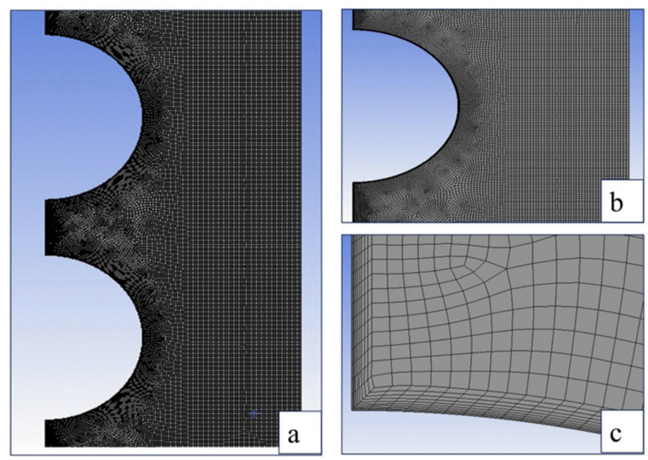

Figure 3. Mesh details **(a)** In-line double tube **(b)** Single tube **(c)** Zoomed view (Inflation layer shown)

4. Methodology

4.1. Solver settings and operating conditions

The Volume of Fluid (VOF) multiphase model is used for simulation, in conjunction with a pressure-based transient solver that employs the Pressure Implicit-Splitting of Operators (PISO) method. The Geo-reconstruct Volume Fraction discretization scheme was used. The simulation utilized water density (ρ_w = 998 kg/m³), viscosity (μ_l = 0.001 Pa.s), and surface tension coefficient (0.072 N/m) under normal temperature and pressure conditions. The variable step size ranged from $1x10^{-3}$ to $1x10^{-6}$, with an absolute convergence criterion of $1x10^{-6}$ chosen for the simulation. The VOF model is preferred to dynamically detention the interface of two-phase (gas-liquid) flow and to define the flow boundary of the liquid film. This method defines the vapour-liquid boundary by computing the volume portion of each phase in every grid cell. A specific area has been patched, and the solution is initialized from the inlet boundary. A cut-off volume fraction of 0.5 is usually considered to distinguish the boundary between the liquid and vapour (gaseous) phases. Key parameter selections and their assigned values are presented in Table 1.

Table 1. Parametric selection and assigned values

S. N.	Parametric selection	Assigned methods/value
1	Multiphase model	Volume of fluid (VOF)
2	Solver type	Pressure based
3	Pressure velocity coupling	PISO
4	Discretization scheme	Geo-reconstruct
5	Surface tension (water-air)	0.072 (N/m)
6	Time step size (variable)	$1x10^{-3} < t > 1x10^{-6}$
7	Time frame	Transient
8	Pressure outlet/inlet	1 atm

4.2. Grid independence test

With all flow and fluid properties kept constant, the film thickness at β = 90° has been evaluated with different grid sizes of 57,505, 46,576, and 31,462 cells and the results were compared across these grids. It was observed that there was no considerable variation in the outcome as the number of cells increased, as shown in Table 2. Therefore, the domain was divided into 31,462 cells to optimize the computational resources for subsequent simulations.

Table 2. Film thickness with different grid points

No of Grid	57505	46576	31462
Film Thickness (δ) (mm) at β = 90°	0.42342	0.42312	0.42318

For the selected number of cells, an acceptable and satisfactory minimum skewness of 1.3×10^{-10} has been achieved, and the maximum orthogonal quality approaches 1. The maximum and minimum aspect ratios are 19.5 and 1, respectively. These parameters indicate that the generated mesh is acceptable as a high-quality grid suitable for accurate CFD simulations. During the grid independence test, the Y^+ value was also determined according to the first cell height. It was computed using the wall shear stress, fluid viscosity, and fluid density. The resulting mesh is sufficiently fine to capture minor flow variations, with a Y^+ value of 0.705.

4.3. Governing equations

The governing equations for the conservation of mass and momentum are presented as equations (1), (2) and (3). The material conservation equation, along with the volume fraction equations used to capture the liquid–gas interface, are provided as equations. (4), (5) and (6). The proposed Nusselt number correlation, developed based on the numerical simulation results, is presented in Eq. (7).

Mass conservation:

$$\frac{\partial \rho}{\partial t} + \nabla.(\rho\vec{V}) = 0 \tag{1}$$

Equation of momentum:

X- Component:

$$\frac{\partial (\rho u)}{\partial t} + \nabla \cdot (\rho u\vec{V}) = -\frac{\partial p}{\partial x} + \frac{\partial \tau_{xx}}{\partial x} + \frac{\partial \tau_{yx}}{\partial y} + \rho f_x \tag{2}$$

Y- Component:

$$\frac{\partial (\rho v)}{\partial t} + \nabla \cdot (\rho v\vec{V}) = -\frac{\partial p}{\partial y} + \frac{\partial \tau_{xy}}{\partial x} + \frac{\partial \tau_{yy}}{\partial y} + \rho f_y \tag{3}$$

Material Equation:

$$\frac{\partial (\alpha)}{\partial t} + \vec{\nu}.\nabla \alpha = 0 \tag{4}$$

Volume Fraction Equation:

$$\rho = \alpha_l \rho_l + \alpha_G \rho_G \tag{5}$$

$$\mu = \alpha_l \mu_l + \alpha_G \mu_G \tag{6}$$

Nusselt (1916) Correlation for film thickness:

$$(\delta) = \left(\frac{3\mu_L \Gamma}{\rho_L(\rho_L - \rho_G) g \sin\beta}\right)^{\frac{1}{3}} \tag{7}$$

5. Results and discussion

5.2. Model validation

The method typically starts with a liquid feed entering the upper portion of the tube. The fluid is evenly distributed across the surface, forming a thin film that flows downward due to gravity. [30] presented a robust methodology based on the fractional Volume of Fluid approach, delineating two immiscible fluid flows or flow over a free surface. In the present simulation, this VOF model has been employed. The fluid domains have been discretized with volume of fractions (α_l=1, α_a=0) for liquid and air.

A fluctuating behavior of film thickness adversely affects the consistency of the film evaporation in evaporative heat exchangers. Hence, it is crucial to investigate the behavior of film thickness formation over the circumference of the tube. This paper distinctly captures and presents the revelation of the transient behavior of film flow over the surface of a tube.

Figure 4 (a) & (b) illustrate a fully developed flow around the tube's circumference. The flow fields around the circumference of the tube are classified into four zones, as depicted in Figure 4 (b). The first zone (I) corresponds to the impingement zone within the flow domain, where the liquid initially impacts on the upper section of the tube. In this region, the formation of the film and its thickness exhibit considerable fluctuations. Consequently, the variations in thickness are not considered in this zone for further discussion. Following this, the second (II) and third zones (III) pertain to the developing and developed flow. The final category one is the detachment zone (IV), where the flow begins to separate from the surfaces of the tube.

In the present investigation, the outcomes were initially verified using the correlation proposed by [6] and a non-invasive optical measurement technique employed by [5] to investigate the allocation of the liquid film thickness around the circumference of the tube.

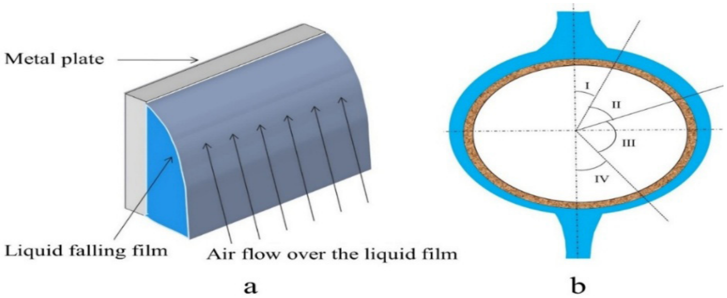

Figure 4. Schematic view of film formation **(a)** Sectional view **(b)** Full view of the domain (Zones: I- Impingement, II Developing, III- Developed, IV- Detachment)

The chosen tube diameter (D_o=19.05mm) is typically utilized in the design of evaporative heat exchangers for commercial applications. In comparison to fluctuating tube diameters under similar parameters, the variation in film thickness is more consistent around the circumference of the tube. This behavior has also been noted in both experimental studies conducted by [31] and numerical simulations performed by [17].

The distribution of liquid film thinness is strongly linked to its position along the circumference, which directly governs both the direction and magnitude of the tangential ($F_{g,t}$) and radial ($F_{g,r}$) components of gravity (F_g), as depicted in Figure 5. On the apex tube section, the tangential element of gravity ($F_{g,t}$) begins at zero when the circumferential position is 0°, gradually increasing to its maximum at 90°. The radial factor of gravity ($F_{g,r}$) is countered by the normal force (F_n) exerted by the tube surface, along with adhesive force (F_a) and surface tension (F_σ) within the fluid. Meanwhile, the tangential factor of gravity ($F_{g,t}$) is counteracted by viscous drag (F_μ), which opposes the flow direction.

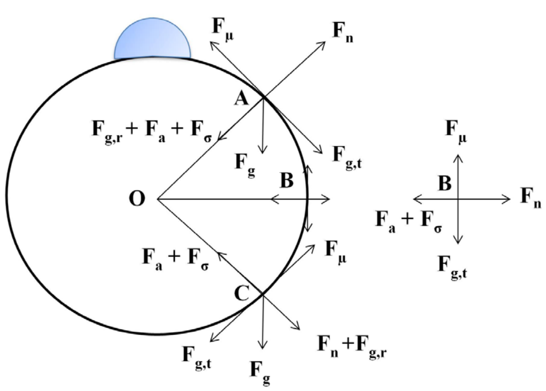

Figure 5. Analysis of forces

The film thickness exhibits more fluctuations in both the impact zone and the detachment zone. This paper focuses on analyzing the instability and transitional behavior of film thickness in these zones. The novelty of this paper lies in visualizing the flow domains and gaining an improved understanding of the fundamentals of formation of liquid film instability and surface heat transfer characteristics over the tube surface under gravity-driven flow. This research aims to reduce reliance on costly experimental investigations that have been consistently used and instead adopt a reliable numerical approach. The analysis is conducted with an outer tube diameter (D_o) of 19.05mm, tube spacing (S) set at 6.4mm, and film Reynolds numbers (Re_f) of 850 & 1050. Under fully developed flow conditions, the film thickness around the specified circumferential positions has been simulated. A comparison of the results available in the literature is shown in Figure 6. The results at film Reynolds number of Re_f = 574 are equated with the available findings of [6] correlation and [5], and it is further extended with the extended film Reynolds numbers of Re_f = 850 and 1050 on a single validation graph. The observed variations are within the acceptable limit. However, it is worth noting that the analysis does not consider the variation in liquid film thickness near the stagnation zone (0° to 20°) and detachment zone (160° to 180°) of the tube's circumference. This exclusion is deliberate because abnormal film thicknesses were observed in this circumferential position. Figure 6 shows that the film thickness at Re_f = 1050 is consistently higher than that at Re_f = 850 for all angular positions around the tube, with an average reduction of 6.26%. The trend in both flows indicates a gradual decrease in film thickness with increasing circumferential position up to the range of 100°–120°, after which it begins to increase until the detachment point. This behavior is attributed to the combined effects of tube curvature, surface tension, and centrifugal forces acting on the flow.

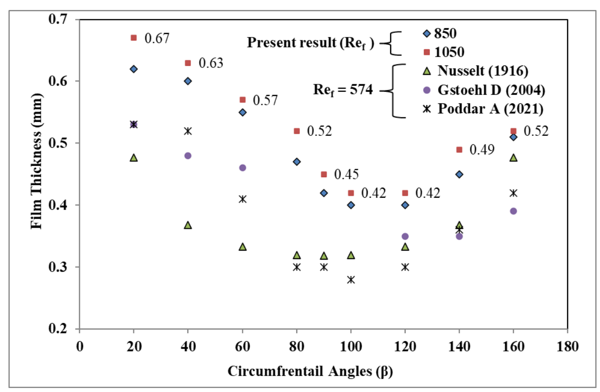

Figure 6. Film thickness variation around the circumference of the tube

5.3. Numerical investigation

5.2.1. Transitional behavior of film fluctuations

In this section, a comprehensive portrayal of a descending liquid film is presented. Figure 7 (a) elucidates the evolution of the film by enveloping two horizontally aligned circular tubes. Notably, a distinct void arises at the corner of the tubes, as presented in the zoomed view in Figure 7 (b), indicating the parting of the liquid film from the surface in these areas. Furthermore, Figure 7 (c) illustrates the allotment of velocity vectors surrounding the surface of the tubes.

Figure 8 elucidates the outline of the mixture interface, clearly displaying stagnation points, thereby providing a distinct visual representation. Additionally, it is worth observing that the least observable film thickness is achieved for the circumferential angles ranging from 100° to 120°.

Figure 9 depicts the fluctuation in liquid film thickness over the surface of the tube. The film thickness, observed at surface angular position of $\beta = 60^{o}$, 90^{o} & 120^{o} from the tube's top, is examined over time for a tube with a diameter of D_o = 19.05mm and a spacing of s = 6.4mm. The plotted data represent averaged values derived from the circumferential profile of the tube surfaces. Specifically, the liquid thickness at this circumferential position is considered after a flow duration of 0.15s to ensure coherent behavior. The curve displayed exhibits asymptotic behavior in film thickness for all angles after 0.3s. The transient film thicknesses exhibit coherence, indicating a uniform and stable liquid distribution over time. This coherence minimizes fluctuations in the local film profile, reducing the potential formation of dry patches on the heat transfer surface. As a result, the continuous wetting of the surface ensures improved heat transfer performance and prevents localized overheating.

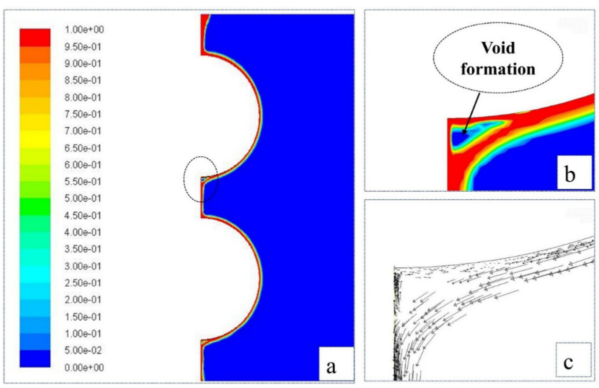

Figure 7. Liquid film flow contours **(a)** Full domain **(b)** Enlarged view **(c)** Vector plot

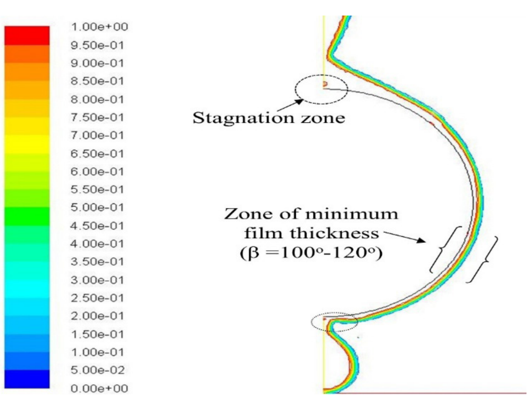

Figure 8. Liquid–surrounding interface flow

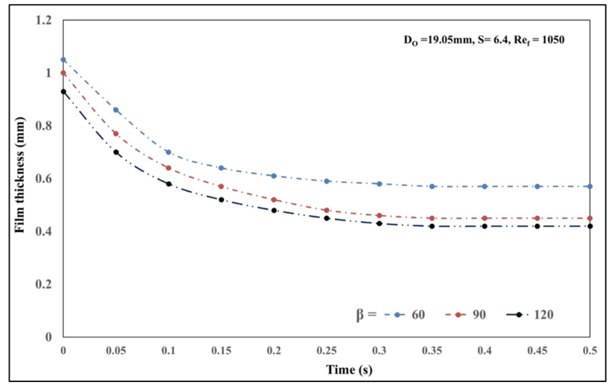

Figure 9. Transient film thickness around the circumference of the tube with respect to time

5.2.2. Flow contours

The velocity vectors illustrating the boundary layer development around the tube surface are shown in Figure 10. The full flow domain with velocity vectors is shown in Figure 10 (a), where Figure 10 (b) and (c) depict a closer view of the top surface and formation of boundary layer on the solid surface, respectively. The recirculation zones observed around the tube depicted in Figure 11 result from the separation and reversal of the flow field in these regions.

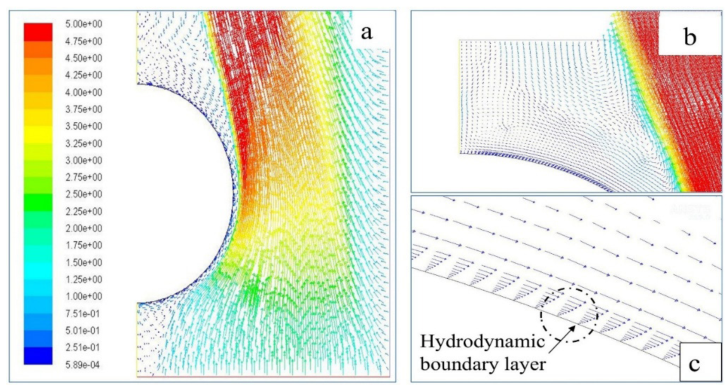

Figure 10. **(a)** Velocity vectors **(b)** Top view **(c)** Development of boundary layer

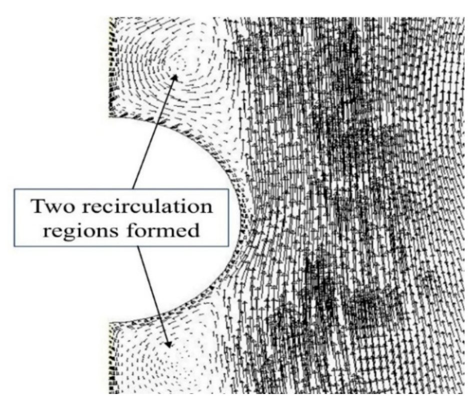

Figure 11. Velocity vector plot

5.2.3. Wall shear stress

Figure 12 illustrates the shear stress over the surface of the tube, and its distribution along the surface. Significant fluctuations are evident, particularly in the vicinity of the tube's impingement zone, with analogous behavior observed near its base. A gradual progression of fluctuations is observed between these regions. In the initial contact zone, fluid meets the tube surface, where it momentarily reaches zero velocity before being compelled to flow around the tube by the inertial force of gravity. The maximum wall surface shear stress is reached near the tube's detachment zone.

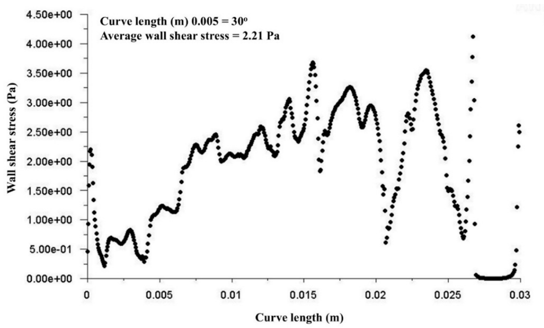

Figure 12. Fluctuating wall shear stress (mixture) vs. Curve length (Time: 0.35s)

5.4. Heat transfer characteristics over the tube surface

5.3.1. Mechanism of heat interaction with the falling liquid film

In the current numerical simulation, heat interaction is considered as a constant surface heat flux on the tube outer surface. Figure 13 illustrates the mechanism of heat interaction with the falling liquid films.

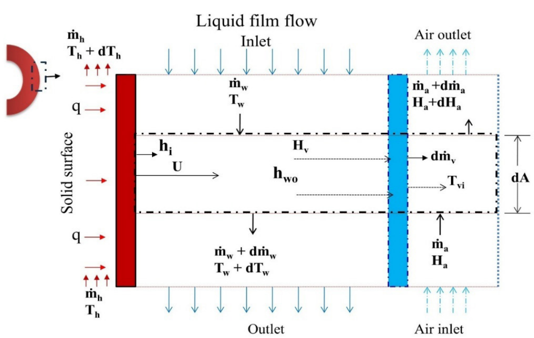

Figure 13. Mechanism of heat interaction with falling liquid film (Form: Curve image)

The energy equation for a gravity-driven liquid film flows over the tube within the control volume is described in Equation (8).

$$\hat{m}_w C_w T_w + U(T_h - T_w)(dA) = (\hat{m}_w + d\hat{m}_w)(C_w)(T_w + dT_w) + (H_v)(d\hat{m}_v) + h_a(T_{vi} + T_a)(dA) \quad (8)$$

[32] proposed a correlation presented in Eq. (9) for the heat transfer rate in the region of nucleate boiling based on experimental observations:

$$\dot{q}_{nucleate} = \mu_l h_{fg}\left[\frac{g(\rho_l - \rho_v)}{\sigma}\right]^{1/2}\left[\frac{c_{pl}(T_s - T_{sat})}{C_{sf} h_{fg} Pr_l^n}\right]^3 \quad (9)$$

There are two alternative methods adopted to enhance the evaporation rate of FFE are to increase the overall surface heat transfer quantity or to increase the thermal potential difference. These two approaches are limited because the evaporation rate can be increased by increasing the thermal potential differences, but on the other side the possibility of film breakdown increases when heat flux increases beyond the operational limit. In another method, a higher heat transfer coefficient can be achieved by increasing the flow rate of flowing liquid. This method increases the use of extra water resources; hence, the economy of operation suffers, and a balanced approach is adopted. This section illustrates the numerical prediction of film heat transfer analysis under a constant surface heat flux (q = 40 kW/m²K), while keeping other variables constant as discussed in the previous section. The future scope of this work includes exploring different heat flux conditions with various parameters. However, for the current study, the analysis is limited to a single variable to maintain conciseness and avoid excessive length. This study specifically investigates the sheet mode of flow within the designated zone.

5.3.2. Surface heat transfer characteristics

Figure 14 illustrates the surface heat interaction contours across the full numerical domain. with parameters set at constant surface heat flux q = 40 kW/m^{2}K, Re_f = 1050, tube diameter D_o = 19.05 mm and S = 6.4mm. It has been investigated that the surface heat transfer coefficient shows a maximum fluctuation (9.21kW/m^{2}K) in the zone of impingement ($0^o \leq \beta \geq 20^o$) and then a continuous variation is shown in the downstream due to the development of thermal boundary layers. The simulation shows that the surface heat-transfer coefficient varies with angular position, thereby also elucidating the local heat-transfer behavior, ranging from 9.21 kW/m²K at the top to 2.15 kW/m²K at the bottom. Despite differences in absolute values, [12] also observed a similar variation in heat transfer with angular position.

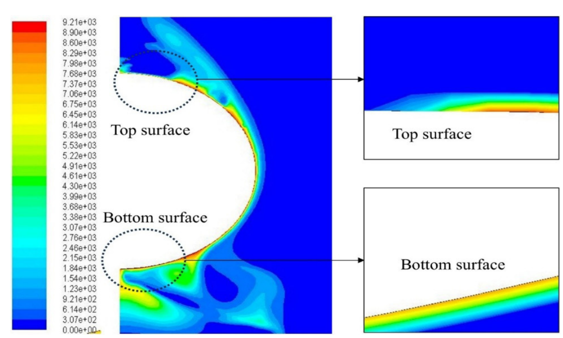

Figure 14. Surface heat interaction contours (kW/m^{2}K) q = 40 kW/m^{2}K, Re_f = 1050, D_o = 19.05 mm and S = 6.4mm)

The simulation was also conducted to analyze the effect of the surface wall heat transfer coefficient for tube diameters of 19.05 mm and 25.04 mm, while keeping flow variables constant. For an enlarged tube diameter, the impingement effect is weaker compared to a smaller tube diameter. This is because, for a larger tube diameter, the reduced surface curvature and the smaller normal velocity component of the falling film led to weaker impingement compared to that on a smaller, more curved tube. However, even with a smaller tube diameter, the variation in the film surface heat transfer coefficient remains insignificant compared to that of a larger tube diameter as depicted in Figure 15. The numerical simulation is further broadened to evaluate the surface heat transfer coefficient for different film Reynolds number as depicted in Figure 16. However, a similar pattern of surface heat transfer coefficients was observed for Reynolds numbers Re_f = 1250, 1050, and 850 across the entire tube surface. It is observed that the surface heat transfer coefficient increases with increasing Re_f, which can be attributed to the enhanced convective effects resulting from higher flow momentum under identical conditions. The highest fluctuations were found in the impingement section of the tube surface, followed by a smoother distribution. The fluctuations observed near the impingement zone arise as the falling film begins to align along the curved surface of the tube, particularly within the 0°-20 circumferential range. In the 20°-160° circumferential range, the maximum variation in the surface heat-transfer coefficient between film Reynolds numbers of 1250 and 1050 is limited to 11% while for Reynolds numbers 1050 and 850, the variation is 15%.

The detachment region exhibits a chaotic flow pattern, which also contributes to fluctuations in the tail zone (160°-180°). A similar fluctuation behavior has been carefully addressed by [12] to improve predictive accuracy.

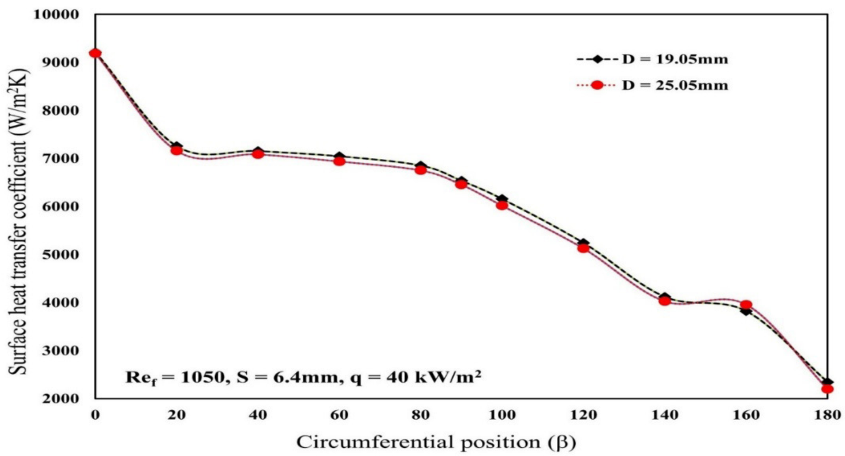

Figure 15. Surface heat transfer coefficient for tube diameters of 19.05 mm and 25.05 mm

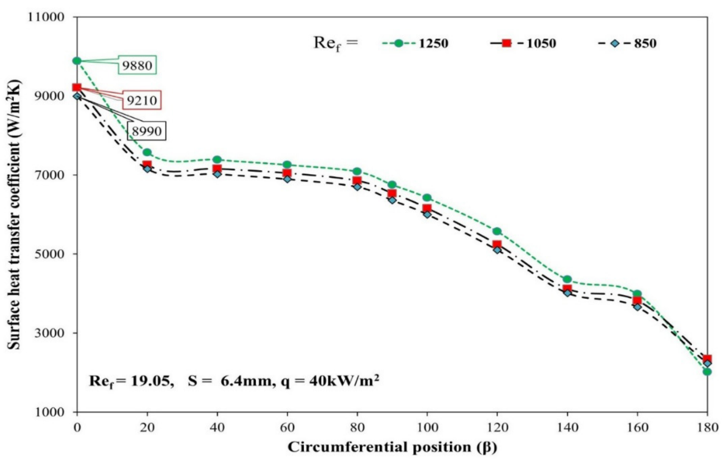

Figure 16. Surface heat transfer coefficient for different film Reynolds numbers

6. Conclusion

Utilizing the ANSYS Fluent CFD software, simulations were conducted to visualize the liquid film flow patterns around horizontal round tubes in a falling film evaporative heat exchanger. For tubes of diameters 19.05 mm & 25.05mm, simulations were carried out for three liquid film Reynolds numbers (Re_f = 850, 1050 & 1250), other fluid properties being held constant. The visualization of flow around the round tubes was effectively captured, and the flow behavior was examined along the outer curvature of the tubes. It was observed that as the film Reynolds number increased, the thickness of the film surrounding the tube also grew; there was a concurrent rise in the likelihood of void formation on the bottom of the tube. The fluctuating behavior of film formation around the tube arrangements was distinctly identified. It was seen that the surface wall shear stresses and surface heat transfer coefficient near the impingement zone exhibit significant instability, showing abnormal fluctuations which can be attributed to the impingement effect. It is concluded that the current simulation approach accurately predicts the phenomena involved and is sufficiently robust to accommodate the possible variations introduced in the study.

The current two-dimensional study of falling film evaporation analyzes flow and geometrical effects on film behavior and heat transfer but omits phase transition due to its complexity. Future work will focus on three-dimensional simulations incorporating both heat and mass transfer during phase transition.

Authors contributions

Poddar AK: Conceptualization, investigation, and writing original draft; Singh NK: Reviewing and supervision.

Declaration of interest

The authors report there are no competing interests to declare.

Data availability

The raw data supporting the findings of this study are available from the corresponding author upon reasonable request.

AI-assisted writing declaration

Limited generative AI was used only for language editing and grammar improvement.

Nomenclature

C	Specific heat ($kJkg^{-1}K^{-1}$)
c_{pl}	Specific heat of the liquid, J/(kg·°C)
C_{sf}	Experimental constant
dA	Control volume (m^2)
Fa	Adhesive force
F_G	Gravitational force
F_{Gt}	Tangential components of force
F_{Gr}	Radial components of force
F_n	Normal force (N)
F_μ	Viscous drag
F_σ	Surface tension
g	Gravitational acceleration, m/s^2
H_a	Enthalpy of dry air ($kJ.kg^{-1}$)
hi	Heat transfer coeff.t at inner side of liquid film ($kW.m^{-2}.K^{-1}$)
h_{wo}	Heat transfer coeff. at outer interface of liquid ($kW.m^{-2}.K^{-1}$)
H_v	Enthalpy of vapor ($kJ.kg^{-1}$)
h_{fg}	Enthalpy of vaporization, J/kg
$\dot{m}_a$	Mass flow rate of dry air at inlet of the evaporator ($kg.s^{-1}$)
$\dot{m}_v$	Mass flow rate of vapour at inlet of the evaporator ($kg.s^{-1}$)
$\dot{m}_w$	Mass flow rate of distributed water at inlet ($kg.s^{-1}$)
$\dot{m}_h$	Mass flow rate of hot water at inlet ($kg.s^{-1}$)
Pr	Prandtl number of the liquid
q	Heat flux (W/m^2)
T_{vi}	Temperature of the vapor-water interface (°C)
T_w	Temperature of the distributed water (°C)
T_h	Temperature of the hot water (°C)
T_s	Surface temperature of the heater, °C
T_{sat}	Saturation temperature of the fluid, °C
U	Overall heat transfer coefficient ($kW.m^{-2}.K^{-1}$)
Γ	Film flow per unit width ($\dot{m}/\pi D$), (kg/ms)
μ_l	Viscosity of the liquid, kg/(m·s)
ρ_l	Density of the liquid, kg/m^3
ρ_v	Density of the vapor, kg/m^3
σ	Surface tension of the interface, (N/m)

References

[1] BOUMAN S, WAALEWIJN R, JONG P DE, LINDEN HJLJV DER. Design of falling-film evaporators in the dairy industry. Int J Dairy Technol 1993;46. https://doi.org/10.1111/j.1471-0307.1993.tb01256.x.

[2] Armbruster R, Mitrovic J. Evaporative cooling of a falling water film on horizontal tubes. Exp Therm Fluid Sci 1998;18. https://doi.org/10.1016/S0894-1777(98)10033-X.

[3] Ji WT, Zhao CY, Zhang DC, Yoshioka S, He YL, Tao WQ. Effect of vapor flow on the falling film evaporation of R134a outside a horizontal tube bundle. Int J Heat Mass Transf 2016;92. https://doi.org/10.1016/j.ijheatmasstransfer.2015.09.023.

[4] Cyklis P. Industrial scale engineering estimation of the heat transfer in falling film juice evaporators. Appl Therm Eng 2017;123. https://doi.org/10.1016/j.applthermaleng.2017.05.194.

[5] Gstoehl D, Roques JF, Crisinel P, Thome JR. Measurement of falling film thickness around a horizontal tube using a laser measurement technique. Heat Transfer Engineering 2004;25. https://doi.org/10.1080/01457630490519899.

[6] NUSSELT W. Die oberflachenkondensation des wasserdamphes. VDI-Zs 1916;60:541.

[7] Zhang JT, Wang BX, Peng XF. Falling liquid film thickness measurement by an optical-electronic method. Review of Scientific Instruments 2000;71. https://doi.org/10.1063/1.1150557.

[8] Chen J, Zhang R, Niu R. Numerical simulation of horizontal tube bundle falling film flow pattern transformation. Renew Energy 2015;73. https://doi.org/10.1016/j.renene.2014.08.007.

[9] E. DA. Characteristics of Flow in Falling Liquid Films. Chem Eng Proc 1952;48:557–63.

[10] Abraham R, Mani A. Heat transfer characteristics in horizontal tube bundles for falling film evaporation in multi-effect desalination system. Desalination 2015;375. https://doi.org/10.1016/j.desal.2015.06.018.

[11] Wang X, He M, Fan H, Zhang Y. Measurement of falling film thickness around a horizontal tube using laser-induced fluorescence technique. J Phys Conf Ser 2009;147. https://doi.org/10.1088/1742-6596/147/1/012039.

[12] Liu S, Mu X, Shen S, Li C, Wang B. Experimental study on the distribution of local heat transfer coefficient of falling film heat transfer outside horizontal tube. Int J Heat Mass Transf 2021;170. https://doi.org/10.1016/j.ijheatmasstransfer.2021.121031.

[13] Zhou Y, Cai Z, Ning Z, Bi M. Numerical simulation of double-phase coupled heat transfer process of horizontal-tube falling film evaporation. Appl Therm Eng 2017;118. https://doi.org/10.1016/j.applthermaleng.2017.02.101.

[14] Zhao CY, Ji WT, Jin PH, Zhong YJ, Tao WQ. Experimental study of the local and average falling film evaporation coefficients in a horizontal enhanced tube bundle using R134a. Appl Therm Eng 2018;129. https://doi.org/10.1016/j.applthermaleng.2017.09.135.

[15] Liu ZH, Yi J. Falling film evaporation heat transfer of water/salt mixtures from roll-worked enhanced tubes and tube bundle. Appl Thermal Eng 2002;22. https://doi.org/10.1016/S1359-4311(01)00061-8.

[16] Pu L, Li Q, Shao X, Ding L, Li Y. Effects of tube shape on flow and heat transfer characteristics in falling film evaporation. Appl Thermal Eng 2019;148. https://doi.org/10.1016/j.applthermaleng.2018.11.043.

[17] Singh N, Poddar AK. Numerical Study of Liquid Film Formation around Tubes of Horizontal Falling Film Evaporator. Journal of Applied Fluid Mechanics 2021;14:1045–52.

[18] Al Jibory (1) M, Rashid FL, Talib SM. Numerical investigation of heat transfer enhancement in ribbed elliptical passage. Journal of Engineering and Applied Sciences 2018;3:313–29.

[19] Al Jibory (2) MW, Rashid MW, Alais SMA. An Experimental and numerical investigation of heat transfer enhancement using annular ribs in a tube. IOP Conf Ser Mater Sci Eng 2018;433:012057. https://doi.org/10.1088/1757-899X/433/1/012057.

[20] Wan Z, Li Y, Wang S. A comprehensive simulation and optimization on heat transfer characteristics of subcooled seawater falling film around elliptical tubes. Appl Thermal. Eng 2021;189. https://doi.org/10.1016/j.applthermaleng.2021.116675.

[21] Dai Z, Zhang Y, Wang S, Nawaz K, Jacobi A. Falling-film heat exchangers used in desalination systems: A review. Int J Heat Mass Transf. 2022;185. https://doi.org/10.1016/j.ijheatmasstransfer.2021.122407.

[22] Han H, Su Z, Du Y, Wang J, Li Y, Liu L, et al. Numerical study on the effect of surface wettability on the falling film flow characteristics of the spiral wound tube heat exchanger. Chemical Engineering Research and Design 2023;190. https://doi.org/10.1016/j.cherd.2022.12.018.

[23] Gönül A, Okbaz AB. Enhanced performance of a microchannel with rectangular vortex generators. Journal of Thermal Engineering 2023;9:260–78. https://doi.org/10.18186/thermal.1272395.

[24] Rahman MA, Dhiman SK. Thermo-fluid performance of a heat exchanger with a novel perforated flow deflector type conical baffles. Journal of Thermal Engineering 2024;10:868–79. https://doi.org/10.14744/thermal.0000846.

[25] SINGH U, GUPTA NK. Thermal performance analysis of heat pipe using response surface methodology, Udayvir. Journal of Thermal Engineering 2023:411–23. https://doi.org/10.18186/thermal.1277897.

[26] Barai R, Kumar D, Wankhade A. Heat transfer performance of nanofluids in heat exchanger: a review. Journal of Thermal Engineering 2023;9:86–106. https://doi.org/10.18186/thermal.1243398.

[27] Shah AH, Memon LA, Luhur MR, Jamali QB, Bhangwar SH, Rajput UA. Performance and fluid flow analysis of double pipe heat exchanger using AL2O3-nanofluid. Journal of Thermal Engineering 2024;10:1120–36. https://doi.org/10.14744/thermal.0000855.

[28] Zhao CY, Zheng CM, Wang XS, Qi D, Jiang JM, Ji WT, et al. Correlations of falling film hydrodynamics and heat transfer on horizontal tubes: A review. Renewable and Sustainable Energy Reviews 2024;197. https://doi.org/10.1016/j.rser.2024.114384.

[29] Zhang W, Niu B, Liu Z, Wang Z. Numerical investigation on heat transfer enhancement of falling film evaporation by surface structure optimization. Desalination Water Treat 2025;322:101073. https://doi.org/10.1016/j.dwt.2025.101073.
[30] Hirt CW, Nichols BD. Volume of fluid (VOF) method for the dynamics of free boundaries. J Comput Phys 1981;39. https://doi.org/10.1016/0021-9991(81)90145-5.
[31] Hou H, Bi Q, Ma H, Wu G. Distribution characteristics of falling film thickness around a horizontal tube. Desalination 2012;285. https://doi.org/10.1016/j.desal.2011.10.020.
[32] Rohsenow WM. METHOD OF CORRELATING HEAT-TRANSFER DATA FOR SURFACE BOILING OF LIQUIDS. American Society of Mechanical Engineers, Heat Transfer Division, (Publication) HTD, vol. 57, 1986. https://doi.org/10.1115/1.4015984.